Atmos. Meas. Tech. Discuss., 7, 1807–1833, 2014
www.atmos-meas-tech-discuss.net/7/1807/2014/
doi:10.5194/amtd-7-1807-2014

Atmospheric Measurement Techniques
Discussions
Open Access

Automated rain rate estimates using the Ka-band ARM Zenith Radar (KAZR)

A. Chandra[1], C. Zhang[1], P. Kollias[2], S. Matrosov[3], and W. Szyrmer[2]

[1]Rosenstiel School of Marine and Atmospheric Sciences, University of Miami, Miami, Florida, USA
[2]Department of Atmospheric and Oceanic Sciences, McGill University, Montreal, Canada
[3]Cooperative Institute for Research in Environmental Sciences, University of Colorado and NOAA/Earth System Research Laboratory, Boulder, Colorado, USA

Received: 14 January 2014 – Accepted: 1 February 2014 – Published: 25 February 2014

Correspondence to: A. Chandra (achandra@rsmas.miami.edu)

Published by Copernicus Publications on behalf of the European Geosciences Union.

Abstract

The use of millimeter wavelength radars for probing precipitation has recently gained interest. However, estimation of precipitation variables is not straightforward due to strong attenuation, radar receiver saturation, antenna wet radome effects and natural microphysical variability. Here, an automated algorithm is developed for routinely retrieving rain rates from profiling Ka-band (35-GHz) ARM zenith radars (KAZR). A 1-D simple, steady state microphysical model is used to estimate the impact of microphysical processes and attenuation on the profiles of the radar observables at 35-GHz and thus provide criteria for identifying when attenuation or microphysical processes dominate KAZR observations. KAZR observations are also screened for saturation and wet radome effects. The proposed algorithm is implemented in two steps: high rain rates are retrieved by using the amount of attenuation in rain layers, while lower rain rates by the Z_e–R (reflectivity-rain rate) relation is implemented. Observations collected by the KAZR, disdrometer and scanning weather radars during the DYNAMO/AMIE field campaign at Gan Island of the tropical Indian Ocean are used to validate the proposed approach. The results indicate that the proposed algorithm can be used to derive robust statistics of rain rates in the tropics from KAZR observations.

1 Introduction

In the tropics, precipitation is produced from a wide range of cloud systems including precipitating shallow cumuli, congestus, deep convective and mesoscale convective systems (Houze, 2004). Observations of all clouds and associated precipitation are needed to improve our understanding of the interaction between shallow and deep convection and their roles in the tropical large-scale circulation (Yoneyama et al., 2013). At the same time, macro- and micro-scale structures of cloud and precipitation systems span over a large range of spectrum. Holistic, continuous observations across the scales of time, space and intensity are not easy to collect even at heavily instrumented

AMTD
7, 1807–1833, 2014

sites (Mather and Voyles, 2012). More often than otherwise, only parts of the systems are observed.

This is particularly true in the tropics where weather radar networks are extreme rare and information of precipitation systems comes from active and passive space measurements, ground-based at few long-term monitoring sites, and during special field campaigns (Long et al., 2013). Tropical Rainfall Measurements Mission (TRMM, Kummerow et al., 1998) has collected observations of tropical rainfall that allow climatology of tropical precipitation for more than 10 yr (Wang et al., 2013). NASA's CloudSat Cloud Profiling Radar (Lebsock and L'Ecuyer, 2011) provided unprecedented details of tropical cloud and precipitation. Multi-satellite based precipitation products yield information at finer temporal scales (Huffman et al., 2007). However, shallow and light precipitation remains a challenge for remote sensing measurement from space.

Since the 1990s, the US Department of Energy (DOE) Atmospheric Radiation Measurements (ARM) program has established Tropical Western Pacific sites on Los Negros Island of Manus, Papua New Guinea (1996), on Nauru Island, Republic of Nauru (1998), and at Darwin, Northern Territory, Australia (2002). At these sites, the ARM program operates profiling Millimeter-wavelength Cloud Radars (MMCR) of 35-GHz (Moran et al., 1998; Kollias et al., 2007a). The MMCR offers very high sensitivity and high temporal and spatial resolutions for observations of low-level non-precipitating (both shallow and stratus clouds) and high-level cirrus clouds because of its sensitivity to probe small cloud droplets and ice particles (Clothiaux et al., 2000; Kollias et al., 2007).

In heavy precipitation, MMCR observations are limited due to strong attenuation by raindrops and radar receiver saturation in the lowest 1–2 km. Nevertheless, recent studies (e.g., Aydin and Daisley, 2002; Matrosov, 2005, 2007) have demonstrated the use of millimeter wavelength cloud radars for retrieving rain rates during stratiform conditions using attenuated information in the rain layer. Ka-band radars are able to monitor transitions from shallow non-precipitating to precipitating clouds, which is impossible for traditional precipitation radars (e.g., C-band).

AMTD
7, 1807–1833, 2014

Extending and complementing the attenuation-based technique of estimating rain rates using Ka-band radar observations can help in:

1. Probing cloud and precipitation from a single platform that allows observations of cloud and precipitation as a continuous spectrum. Evolution in cloud population is closely associated with many phenomena, especially in the tropics. Deployment of multiple radars for separated retrieval of precipitation from different cloud systems is feasible only in few special arrangements.

2. Retrieving precipitation from ka-band radars would be useful for many scientific applications to shallow clouds such as, their cloud microphysical parameters, radiation variables, and phase transitions, which have significant impact on diabatic heating profiles of shallow clouds.

3. Deriving long-term precipitation climatology at the DOE ARM Manus site where more than 10 yr of MMCR observations have been collected. This would be a valuable independent data set for comparison to space-borne precipitation products.

Recent enhancements of radar technology (Mather and Voyles, 2012) have substantially improved the quality of the Ka-band ARM Zenith Radar (KAZR, replaces the old acronym MMCR) measurements. In the context of precipitation measurements, the KAZR offers higher receiver dynamic range that limits receiver saturation. Here, we extend the application of KAZR to routine precipitation retrieval. The rest of the paper is organized as follows. Section 2 describes details of the instruments and dataset. Section 3 introduces the automated algorithm to retrieve rain rates from the KAZR. Section 4 discusses the uncertainties and comparison of KAZR rain rate estimates with other ground-based observing tools. Section 5 gives a summary and conclusions.

AMTD
7, 1807–1833, 2014

2 Instruments and datasets

2.1 Observational setting

The DYNAMO (Dynamics of the Madden–Julian Oscillation)/AMIE (ARM MJO Investigation Experiment) field campaign took place in the tropical Indian Ocean and surrounding regions between 1 October 2011 and 31 March 2012. (Yoneyama et al., 2013). By deploying multiple radars of different frequencies along with surface observations of the ARM Mobile Facility (AMF) at Addu Atoll of the Maldives (Fig. 1), it offered a unique opportunity to study tropical cloud population. The instruments and their specifications are listed in Table 1. The radar triad consisted of the S-Polka, SMART-R and KAZR. The KAZR is a profiling Doppler radar operates at Ka-Band (8.66 mm wavelength), which was located at Gan Island airport as part of the AMF. The S-PolKa is an advanced dual polarimetric and dual wavelength (10 cm for S-Band, and 0.8 cm for Ka Band; Keeler et al., 2000) radar located on Hithadhoo Island (0.63° S, 73.10° E), 8.66 km from the KAZR. Its dual-polarimetric capabilities enables improved precipitation estimates as well as hydrometeor identification, and its dual wavelength capabilities allows retrieval of boundary layer humidity profiles and estimates of cloud liquid water content (Ellis and Vivekanandan, 2010, 2011). The SMART-R is a C-Band (5 cm wavelength; Biggerstaff et al., 2005) scanning Doppler radar located also on Hithadhoo Island (0.61° S, 73.09° E), 9.28 km from the KAZR. The SMART-R observation yields quantitative precipitation estimates over range larger than that of the S-PolKa. Vertical scans over the KAZR, were performed by both S-PolKa (every 15 min) and SMART-R (every 10 min), allowing a direct comparison between the three radars and their combined data (Feng et al., 2013).

2.2 Ka-band ARM Zenith Radar (KAZR)

The new Ka-band ARM Zenith pointing Radars (KAZRs) offers vertical profiles of three Doppler moments (reflectivity, Doppler velocity and spectrum width) at a resolution

AMTD
7, 1807–1833, 2014

of 30 m from near-ground up to 20 km and temporal resolution of 4 s. The specifications of the KAZRs are listed in Table 1. The KAZR systems have higher dynamic range than the MMCRs (∼85 dB compared to ∼65 dB), which enables to avoid early receiver saturation during precipitation. (KAZR data used in this study were taken from the KAZR ARSCL (Active Remote Sensing of Clouds) product from the ARM data archive (www.arm.gov/instruments/kazr). KAZR-ARSCL provides cloud boundaries and best estimate of time-height fields of radar moments. In ARSCL, the KAZR radar observations are corrected for gaseous attenuation and velocity folding and non-significant (non-hydrometeors) are removed. The corrected KAZR measurements along with the observations from the micropulse lidar (MPL), ceilometer, soundings, rain gauge, and microwave radiometer (MWR) are combined to make KAZR-ARSCL in two data streams: one with cloud base and cloud layer boundaries, and the other including additional best-estimate of time-height fields of radar moments, and other fields. Figure 2 shows an example of KAZR moments during a stratiform rain event. The sharp gradients of reflectivity and Doppler velocity at ∼5 km indicate the presence of the melting layer. The KAZR is heavily attenuated for high rain rate episodes are seen in the reflectivity field between 01:00–02:00 UTC and 04:00–05:00 UTC. The true cloud top heights corresponding to these high rainfall periods are underestimated due to heavy attenuation.

3 KAZR algorithm of rain rate retrieval

3.1 Physical basis

The development of a automated Ka-band algorithm for the rain rate R (mm h^{-1}) depends on the proper identification of the dominant mechanisms that control the profile of radar reflectivity $Z_{\mathrm{e_{dBZ}}}$ (decibels of mm^6 m^{-3}) and its gradient $\frac{\Delta Z_\mathrm{e}}{\Delta h}$ (dB km^{-1}), where h is height. In light rain the evolution of the drop size distribution (DSD) via different microphysical processes (accretion above the cloud base, evaporation below the cloud

AMTD
7, 1807–1833, 2014

base) has a non-negligible impact on the profile of the radar reflectivity $Z_{e_{dBZ}}$. Consequently, the DSD parameters, in particular the concentration parameter. In this case, specific attenuation A (dB km^{-1}) cannot be used and the rain rate R can be calculated from attenuation-corrected reflectivity values using a proper Z_e–R relationship. In moderate rain, measured vertical gradient of reflectivity (i.e attenuation A) is not very sensitive to the details of DSD for a given rain rate, because R and A are approximately proportional to the same moment of the DSD. The fact that R and A are approximately proportional to the same moment of the DSD is explained in detail by Matrosov et al. (2006).

The vertical gradient of the radar reflectivity of the rain DSD is provided by the following expression:

$$\frac{\Delta Z_{e_{dBZ}}}{\Delta h} = -2(A_r + A_c) + \frac{\Delta Z_{e_{dBZ}}}{\Delta h}|_{PRC} \tag{1}$$

where A_r and A_c are the one-way specific attenuation by cloud and rain liquid water respectively, and $\frac{\Delta Z_{e_{dBZ}}}{\Delta h}|_{PRC}$ is the induced vertical gradient of the reflectivity of the rain DSD due to two microphysical processes: accretion above the cloud base and evaporation below the cloud base. Here, a simple 1-D steady state microphysical model that accounts for accretion of cloud droplets and raindrops/evaporation below the cloud base is used to investigate the sensitivity of $\frac{\Delta Z_{e_{dBZ}}}{\Delta h}$ to either microphysical processes or radar signal attenuation by clouds and raindrops. The details of the parameterization of accretion and evaporation in the model are described in Kollias et al. (2011).

Figure 3 shows the vertical gradient of reflectivity due to accretion, evaporation and attenuation as a function of the Doppler velocity (normalized to the ground level). Above the cloud base, a cloud liquid water content amount of 0.2 gm^{-3} is assumed constant with height to estimate the change in the vertical gradient of the radar reflectivity due to accretion. Below the cloud base, a relative humidity of 80 % is assumed to investigate the impact of evaporation on the observed vertical gradient of the radar reflectivity. Finally, the impact of cloud and liquid attenuation is show in Fig. 3. The rain DSD

AMTD
7, 1807–1833, 2014

is assumed to follow the normalized gamma distribution (Illingworth and Blackman, 2002) and several runs for different shape parameter μ and normalized intercept N_w are shown. The appropriate distribution function is given by

$$N(D) = \frac{N_w 0.033(3.67+\mu)^{\mu+4}}{\Gamma(\mu+4)} \left(\frac{D}{D_o}\right)^{\mu} \cdot \exp\left[-(3.67+\mu)\frac{D}{D_o}\right] \quad (2)$$

Equation (2) reduces to the simple exponential with $N_w = N_o$ when $\mu = 0$. D_o is the median volume diameter. From the literature, the reported range of values of N_w is very large (e.g. Anagnostou et al., 2013) and the values of 8×10^5 and $2.5 \times 10^7\,\mathrm{m}^{-4}$ are taken here as the values representatives for the two bounds (or perhaps extremes). The estimated values of the shape parameter μ are mainly between −1 and 5 (e.g. Gorgucci et al., 2002).

The results are presented as a function of the mean Doppler velocity since this is an observable variable and can be used to classify the precipitation profiles. As expected, at low rain rates (mean Doppler velocity less than 4–5 $\mathrm{m\,s^{-1}}$), the microphysical processes that can affect the evolution of the rain DSD with height are the main contributors to the observed vertical gradient of the radar reflectivity. At mean Doppler velocities higher than 5 $\mathrm{m\,s^{-1}}$ attenuation is the primary contributor to the observed Z_e profile and can be used to extract the rain rate. In Fig. 3, all calculations are done using the Mie theory (and only attenuation). The attenuation by cloud is not shown in this figure. The attenuation by liquid water cloud is proportional to the cloud liquid water content with the proportionality factor slightly temperature-dependent (Matrosov et al., 2004).

Matrosov (2005) demonstrated that at 35 GHz there is a nearly linear relation between specific attenuation (A) and R. Matrosov used this relation to retrieve layered–average rain rates from a Ka-Band vertically pointing radar. The important advantage of this method is that the retrieval of the rain rate is independent of radar calibration, as it does not depend on the absolute reflectivity values. The rain rate estimated in a uniform layer of rain is proportional to the height derivative of the reflectivity expressed in

AMTD
7, 1807–1833, 2014

logarithmic units:

$$R(\mathrm{mm\,h^{-1}}) = k(2c)^{-1}\left(\frac{\Delta Z_\mathrm{e}}{\Delta h}\right) \quad (3)$$

where Z_e is reflectivity in logarithmic units, ΔZ_e the difference of reflectivity between the top and bottom of the layer considered, and Δh the depth of the rain layer. The coefficient c is 0.28 dB km^{-1} h^{-1} mm^{-1}. The coefficient k (dimensionless) accounts for changes in the raindrop fall velocity due to changes in air density, ρ, such that k (h) $\approx 1.1\rho(h)^{-0.45}$. Equation (2) assumes that the two-way attenuation effect of the rain layer is dominant compared to reflectivity changes within the layer due to microphysics.

In addition to liquid attenuation (discussed in the next section), at 35 GHz, the attenuation from water vapor, especially in the Tropics, is significant. In the tropical boundary layer the specific humidity can be as high as 20–25 g kg^{-1} and the signal attenuation can reach 0.35 dB km^{-1} ($10^{-0.035}$, or 92 % km^{-1}) at 35 GHz.

3.2 Retrieval algorithm

Figure 4 shows the flow chart that explains the steps taken in retrieving the rain rate R using KAZR observations. First, the presence of rain in the profile is identified if the maximum reflectivity is greater than −10 dBZ. The rain aloft is considered to reach the ground if the average radar reflectivity and mean Doppler velocity in the layer between 200–400 m a.g.l. exceed 10 dBZ and 3 m s^{-1}, respectively.

The next step is to identify the portion of the Z_e profile that saturates the KAZR receiver. KAZR saturation occurs at high rain rates where attenuation is the main contributor to the observed Z_e profile. Thus, we anticipate that the maximum reflectivity will be observed at the lowest KAZR range gate and subsequently, Z_e will decrease with height due to liquid attenuation. If the maximum Z_e is not located at the lowest gate, the maximum radar reflectivity in the lowest 2 km is detected. The rain layers below the first maximum in reflectivity are not taken into account to avoid the KAZR receiver saturation effects.

AMTD
7, 1807–1833, 2014

From Fig. 3, if evaporation effects are dominant, the theoretical maximum limit for droplet's Doppler velocities is $\sim 5\,\mathrm{m\,s^{-1}}$. Above this, the attenuation effects are dominant. The mean Doppler velocity threshold for separating regimes where attenuation effects are dominant is identified from plotting KAZR rain reflectivity values (averaged between 200–400 m a.g.l.) against rain rates from disdrometer (collocated with few meters apart from the KAZR) for different KAZR Doppler velocities as shown in Fig. 6a. For Doppler velocities $< 5\,\mathrm{m\,s^{-1}}$, the drops are considerably small that the attenuation effects can be neglected and the Z_e–R relationship can be reasonably implemented with some caution. Previous studies have also implemented Z_e–R relationships at Ka-band after correcting the reflectivities from profilers and S-band radars (e.g., Tokay et al., 2009). Using mean Doppler velocity threshold ($5\,\mathrm{m\,s^{-1}}$), the total rain events are classified into two main regimes: rain events with dominant attenuation effects, and rain events with negligible attenuation effects. Based on these two approaches, the automated rain rate estimation algorithm is implemented.

3.2.1 *A*–*R* based estimation

Above saturated layers, rain layers are discretized up to 1.5 km with varying depth starting from 500 m for the first layer. For each layer, the reflectivity difference between the top and bottom of the layer and the bulk reflectivity gradients are calculated. The rain layers suitable for the attenuation technique are identified when both the reflectivity difference between the top and bottom of the rain layer and bulk reflectivity gradients in each rain layer are negative in order to minimize the effect of clouds (where the increase in reflectivity due to condensation results in a reflectivity increase with height).

For the attenuation technique to work, it is necessary that the changes in reflectivity in the rain layer due to attenuation are larger compared to changes due to microphysics (non-attenuation). To quantify these relative magnitudes, the reflectivity changes in the rain layer are calculated from both KAZR and collocated S-Pol reflectivity profiles. For the cases where the attenuated effects are larger than the non-attenuated effects, the non-attenuated magnitudes are subtracted from the attenuated reflectivity differences,

AMTD
7, 1807–1833, 2014

there by accounting for the microphysics. For cases where non-attenuated effects are of comparable magnitudes to the attenuated magnitudes are not considered for retrieval. For most cases, if the rain-rate is about or greater than $5\,\mathrm{mm\,h^{-1}}$, the attenuated magnitudes are larger than the non-attenuated magnitudes by a factor of 3–4. Figure 5 shows an example that illustrates reflectivity profiles for applying the A–R based technique to estimate the rain rate. Compared to the S-polka, heavily attenuated KAZR beams (seen as sudden dips in the cloud top heights) for higher rain rate episodes are shown in Fig. 5a and b; this results in underestimation of the cloud-top heights from the KAZR for higher rain rates. Figure 5c and d demonstrates the KAZRs skill to retrieve rain rates from attenuation information (gradient of reflectivity) over non-attenuated profiles from the S-polka. For higher rain rates ($R > 5\,\mathrm{mm\,h^{-1}}$), a near-linear relationship between the gradient of reflectivity due to attenuation and the rain rate is clearly seen in Fig. 5d.

3.2.2 Z_e–R based estimation of the rain rate

The increased dynamic range of the KAZR systems (∼85 dB) compared to the MMCRs (∼60 dB) makes KAZR systems not saturate under light rain conditions. As a result, a Z_e–R relation can be implemented to retrieve low rain rates. Figure 6a shows KAZR reflectivity values (averaged between 200–400 m a.g.l.) and rain rates from the disdrometer as a function of Doppler velocities. Reflectivity values exhibit skill in implementing the Z_e–R relationship; but there is considerable scatter. The increase in Doppler velocities with rain rates provides an additional constraint to eliminate outliers in the reflectivity values and to further refine the Z_e–R relationship. To do this, for different reflectivity bins, the mean and standard deviation of top 25 % of the Doppler velocities are used as a threshold to eliminate the outliers. The reflectivity values are removed if their corresponding Doppler velocities in each bin exceed the threshold. Figure 6b shows the refined Z_e–R relationship after using Doppler velocities as a constraint. The refined Z_e–R relation can be implemented for rain rates up to ∼4–5 $\mathrm{mm\,h^{-1}}$; above that the contribution of large drops starts to dominate (the Mie effect). In the above Z_e–R implementation, it is assumed that the attenuation effects are negligible

AMTD
7, 1807–1833, 2014

for low rain rates. In order to assess the effect of attenuation and to verify the validity of the obtained Z_e–R relationship, the reflectivity values (at Ka-band; $\lambda = 8.66$ mm) are computed from DSDs obtained from a video disdrometer using Mie calculations (Bohren and Hufman, 1983) as

$$Z_{eh} = \lambda^4 \phi^{-5} |(m_w^2 + 2)/(m_w^2 - 1)|^2 \sum_i \langle \sigma_h(D_{ei}) \rangle n_i(D_{ei}) \quad (4)$$

where m_w is the refractive index of water, σ_h (D_{ei}) the Mie backscatter cross section, n_i (D_{ei}) the droplet concentration in ith diameter bin form disdrometer, and the summation is performed over the disdrometer size bins. The computed reflectivity values from DSDs are compared with the KAZR reflectivity values and corrections are applied to the Z_e–R relationship.

4 Rain rate comparison

Rain rates from the KAZR are continuously retrieved in two steps. For low rain rate cases (DV < 5 m s^{-1}), the Z_e–R relationship is applied. For high rain rates (DV > 5 m s^{-1}), attenuation technique is applied.

Figure 7 shows a scatter plot of 1 min averaged rainfall rates from a video disdrometer and the KAZR with their correlation coefficient of 0.632. The comparison is shown for $R > 5$ mm h^{-1} where the A–R relationship is applied. Figure 8 shows the comparison of 1 min averaged rain rates from the KAZR retrieval vs. a rain gauge. The total rain events sampled during the DYNAMO period cover both stratiform and convective rain events. The observed differences can be attributed to the factors such as sampling volume differences between the rain gauge and KAZR, and also uncertainties in applying the A–R and Z_e–R relationships. Nevertheless, the comparison in terms of the time series and scatter plot agrees reasonably well.

Figure 9 shows the comparison of rain rate histograms from the KAZR, S-Polka and Smart-R for three rain cases (stratiform, convective and total) respectively. The

AMTD
7, 1807–1833, 2014

stratiform vs. convective rain rates are based on the bright band signatures near the melting layer from the KAZR. The detection of the bright band is done following the methodology explained in Geerts (2004). Qualitatively, the shape of the histograms matches well with the peak in the convective rain rates, which is relatively higher compared to the peak in the stratiform rain rates. This behavior of convective rain rate peak being higher is due to strong updrafts, which makes rain droplets to grow bigger by riming and results in higher rain rates as also shown in other studies (Steiner, 1995; Deng et al., 2014). The difference in the shape of the histograms is mainly due to the sampling volume differences and the distance between the radars (Table 1).

5 Summary and conclusions

An automated algorithm is developed to retrieve rain rates from profiling Ka-band observations. To the best knowledge of the authors, this is first attempt to extend KAZR observations for routine rain rate retrieval. The algorithm is applicable to the KAZRs of the ARM program and the MIRA-36 Ka-band radars deployed at several research institutions in Europe. The proposed algorithm uses two different method for estimating the rainfall rate: (i) for high rain rates (DV $> 5\,\mathrm{m\,s^{-1}}$), the A–R relationship is applied. (ii) For lower rain rates (DV $< 5\,\mathrm{m\,s^{-1}}$), the Z_e–R relationship is applied. A 1-D microphysical model that accounts for the microphysical processes of accretion and evaporation, and radar attenuation due to liquid is used to infer the criteria for determining if microphysics or attenuation controls the observed KAZR profiles of radar reflectivity.

The proposed algorithm is applied to 4 months of KAZR observations collected during the deployment of the ARM Mobile Facility in the context of the DYNAMO/AMIE field campaign. The KAZR retrieved rain rates are compared with the nearby surface rain gauge and disdrometer measurements. The comparison shows a good agreement with correlation coefficient of 0.63.

The statistics of the Ka-band retrieved rain rates are comparing to those derived from the S-PolKa and SMART-R data. First the observations are decomposed to stratiform

AMTD
7, 1807–1833, 2014

and convective rain events. The shape of the histograms between different radars is consistent with each other and with the previous studies.

The present study sets a framework for retrieving rainfall rates from Ka-band radars using an algorithm with a physical basis. This algorithm will be applied to retrieve rain rates at the other ARM sites to study shallow to deep convection transitions and related microphysical processes.

Acknowledgements. We would like to thank Zhe Feng from Pacific Northwest National Laboratory for sharing the merged radar data for the DYNAMO period. This study was supported by DOE ASR Grant ER65283.

References

Anagnostou, M. N., Kalogiros, J. F., Marzano, S., Anagnostou, E. N., Montopoli, M., and Piccioti, E.: Performance evaluation of a new dual-polarization microphysical algorithm based on long-term x-band radar and disdrometer observations, J. Hydrometeorol., 14, 560–576, 2013.

Aydin, K. and Daisley, S. E. A.: Relationships between rainfall rate and 35 GHz attenuation and differential attenuation: modeling the effects of raindrop size distribution, canting, and oscillation, IEEE T. Geosci. Remote, 40, 2343–2351, 2002.

Biggerstaff, M, I., Wicker, L. J., Guynes, J., Ziegler, C., Straka, J. M., Rasmussen, E. N., Doggett IV, A., Carey, L. D., Schroeder, J. L., and Weiss, C.: The Shared Mobile Atmospheric Research and Teaching Radar: a collaboration to enhance research and teaching, B. Am. Meteorol. Soc., 86, 1263–1274, 2005.

Bohren, C. F. and Huffman, D. R.: Absorption and Scattering of Light by Small Particles, Wiley, New York, 530 pp., 1983.

Clothiaux, E. E., Ackerman, T. P., Mace, G. G., Moran, K. P., Marchand, R. T., Miller, M. A., and Martner, B. E.: Objective determination of cloud heights and radar reflectivities using a combination of active remote sensors at the ARM CART sites, J. Appl. Meteorol., 39, 645–665, 2000.

Deng, M., Kollias, P., Feng, Z., Zhang, C., Long, C., Kalesse, H., Chandra, A. S., Kumar, V., and Protat, A.: Stratiform and convective precipitation observed by multi-wavelength radars during the DYNAMO/AMIE Experiment, J. Appl. Meteorol. Clim., under review, 2014.

Ellis, S. M. and Vivekanandan, J.: Water vapor estimates using simultaneous dual-wavelength radar observations, Radio Sci., 45, doi:10.1029/2009RS004280, 2010.

Ellis, S. M. and Vivekanandan, J.: Liquid water content estimates using simultaneous S and Ka-band radar measurements, Radio Sci., 46, RS2021, doi:10.1029/2010RS004361, 2011.

Feng, Zhe, McFarlane, S. A., Schumacher, C., Ellis, S., and Bharadwaj, N.: Constructing a merged cloud-precipitation radar dataset for tropical convective clouds during the DYNAMO/AMIE Experiment at Addu Atoll, J. Atmos. Ocean. Technol., doi::10.1175/JTECH-D-13-00132.1, 2014.

Geerts, B. and Dawei, Y.: Classification and characterization of tropical precipitation based on high-resolution airborne vertical incidence radar, Part I: Classification, J. Appl. Meteorol., 43, 1554–1566, 2004.

Gorgucci, E., Chandrasekar, V., Bringi, V. N., and Scarchilli, G.: Estimation of raindrop size distribution parameters from polarimetric radar measurements, J. Atmos. Sci., 59, 2373–2384, 2002.

Houze Jr., R. A.: Mesoscale convective systems, Rev. Geophys., 42, RG4003, doi:10.1029/2004RG000150, 2004.

Huffman, G. J., Bolvin, D. T., Nelkin, E. J., Wolff, D. B., Adler, R. F., Gu, G., Hong, Y., Bowman, K. P., and Stocker, E. F.: The TRMM Multisatellite Precipitation Analysis (TMPA): quasi-global, multiyear, combined-sensor precipitation estimates at fine scales, J. Hydrometeorol., 8, 38–55, 2007.

Illingworth, A. J. and Blackman, T. M.: The need to represent raindrop size spectra as normalized gamma distributions for the interpretation of polarization radar observations, J. Appl. Meteorol., 41, 286–297, 2002.

Kollias, P., Albrecht, B. A., and Marks, F.: Why Mie?, B. Am. Meteorol. Soc., 83, 1471–1483, doi:10.1175/BAMS-83-10-1471, 2002.

Kollias, P., Clothiaux, E. E., Miller, M. A., Albrecht, B. A., Stephens, G. L., and Ackerman, T. P.: Millimeter-wavelength radars: new frontier in atmospheric cloud and precipitation research, B. Am. Meteorol. Soc., 88, 1608–1624, doi:10.1175/BAMS-88-10-1608, 2007.

Kollias, P., Szyrmer, W., Remillard, J., and Luke, E.: Cloud radar Doppler spectra in drizzling stratiform clouds, Part II: Observations and microphysical modeling of drizzle evolution, J. Geophys. Res.-Atmos., 116, D13, doi:10.1029/2010JD015238, 2011.

Kummerow, C., Barnes, W., Kozu, T., Shiue, J., and Simpson, J.: The Tropical Rainfall Measuring Mission (TRMM) sensor package, J. Atmos. Ocean Tech., 15, 809–817, 1998.

Lhermitte, R.: Attenuation and scattering of millimeter wavelength radiation by cloud and precipitation, J. Atmos. Ocean Tech., 7, 464–479, 1990.

Lebsock, M. D. and L'Ecuyer, T. S.: The retrieval of warm rain from CloudSat, J. Geophys. Res., 116, D20209, doi:10.1029/2011JD016076, 2011.

Long, C. N., McFarlane, S. A., Del Genio, A. D., Minnis, P., Ackerman, T. P., Mather, J. H., Comstock, J. M., Mace, G. G., Jensen, M., and Jakob, C.: "ARM research in the Equatorial Western Pacific: a decade and counting", B. Am. Meteorol. Soc., 94, 695–708, doi:10.1175/BAMS-D-11-00137.1, 2013.

Mather, J. H. and Voyles, J. W.: The ARM Climate Research Facility: a review of structure and capabilities, B. Am. Meteorol. Soc., 94, 377–392, doi:10.1175/BAMS-D-11-00218.1, 2013.

Matrosov, S. Y.: Attenuation-based estimates of rainfall rates aloft with vertically pointing Ka-band radars, J. Atmos. Ocean Tech., 22, 43–54, 2005.

Matrosov, S. Y.: Potential for attenuation-based estimations of rainfall rate from CloudSat, Geophys. Res. Lett., 34, L05817, doi:10.1029/2006GL029161, 2007.

Matrosov, S. Y., May, P. T., and Shupe, M. D.: Rainfall profiling using Atmospheric Measurement Program vertically pointing 8 mm wavelength radars, J. Atmos. Ocean Tech., 23, 1478–1491, 2006.

Steiner, M. R., Houze Jr., R. A., and Yuter, S. E.: Climatological characterization of three-dimensional storm structure from operational radar and rain gauge data, J. Appl. Meteorol., 34, 1978–2007, 1995.

Tokay, A., Hartmann, P., Battaglia, A., Gage, K. S., Clark, W. L., and Williams, C. R.: A field study of reflectivity and Z-R relations using vertically pointing radars and disdrometers, J. Atmos. Ocean Tech., 26, 1120–1134, 2009.

Wang, J.-J., Alder, R. F., Huffman, G. J., and Bolvin, D.: An updated TRMM composite climatology of tropical rainfall and its validation, J. Climate, 27, 273–284, doi:10.1175/JCLI-D-13-00331.1, 2013.

Yoneyama, K., Zhang, C., and Long, C. N.: Tracking pulses of the Madden–Julian Oscillation, B. Am. Meteorol. Soc., 94, 1871–1891, 2013.

AMTD
7, 1807–1833, 2014

Zhang, C.: Madden–Julian Oscillation: bridging weather and climate, B. Am. Meteorol. Soc., 94, 1849–1870, doi:10.1175/BAMS-D-12-00026.1, 2013.

AMTD
7, 1807–1833, 2014

AMTD
7, 1807–1833, 2014

Automated rain rate estimates using the Ka-band ARM Zenith Radar (KAZR)

A. Chandra et al.

Table 1. Specifications of radars used in this study.

Radar wavelength/frequency	Range, Resolution	Beamwidth, & sensitivity	Remarks
KAZR (8.66 mm/35 GHz)	15 km, 30 m	0.3 deg, −45 dBZ at 1 km	Vertically pointing
S-PolKa (10 cm for S-band, 0.8 cm for Ka-band)	150 km, 150 m	0.91 deg, −30 dBZ at 8.5 km	Scanning: 8 PPIs (0.5 –11 deg) 55 RHIs (0–45 deg) 8.62 km apart from KAZR
SMART-R (5 cm)	150/300 km, 100 m	1.5 deg, −21 dBZ at 10 km	25 PPIs (0.5–33 deg) RHI over KAZR 9.28 km from KAZR

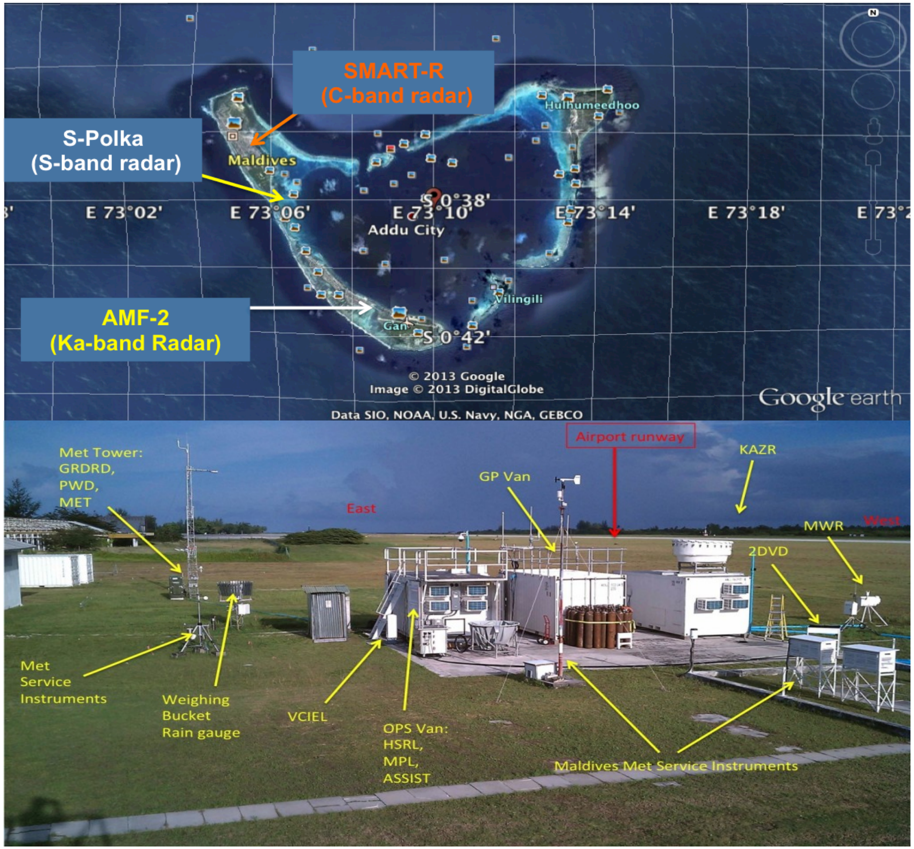

Fig. 1. Top: Aerial view of the radar triad on Addu Atoll during DYNAMO/AMIE. Bottom: AMF-2 Instrument setup at Gan Island during DYNAMO.

AMTD
7, 1807–1833, 2014

Automated rain rate estimates using the Ka-band ARM Zenith Radar (KAZR)

A. Chandra et al.

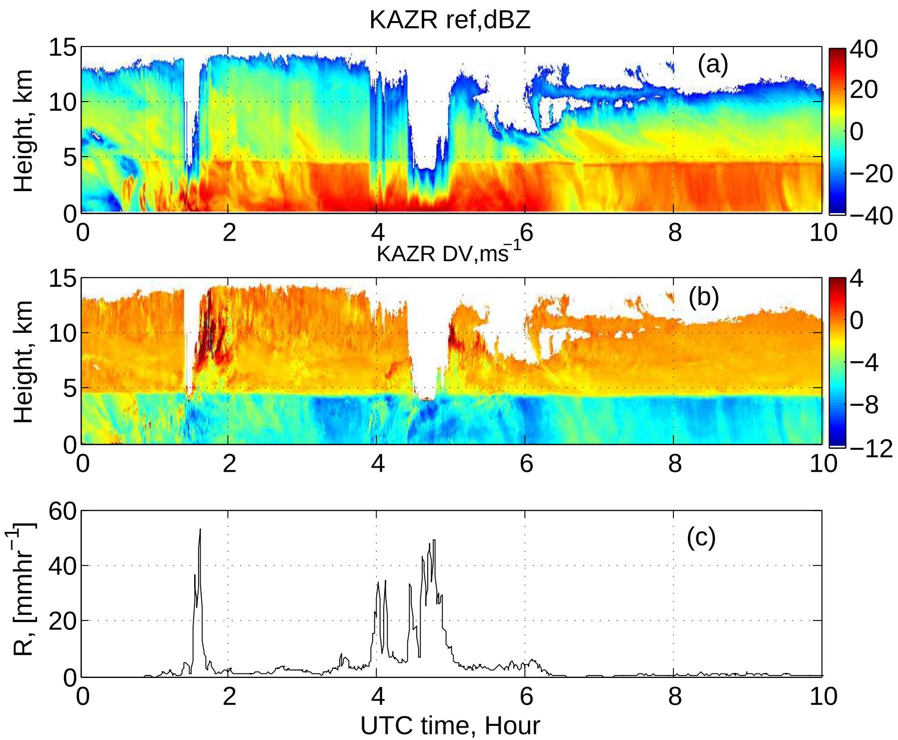

Fig. 2. An example of time-height plots of **(a)**. KAZR reflectivity (dBZ) and **(b)** KAZR mean Doppler velocity (m s^{-1}; -ve for downward). Panel **(c)** shows the surface rain rates from an optical rain-gauge.

AMTD
7, 1807–1833, 2014

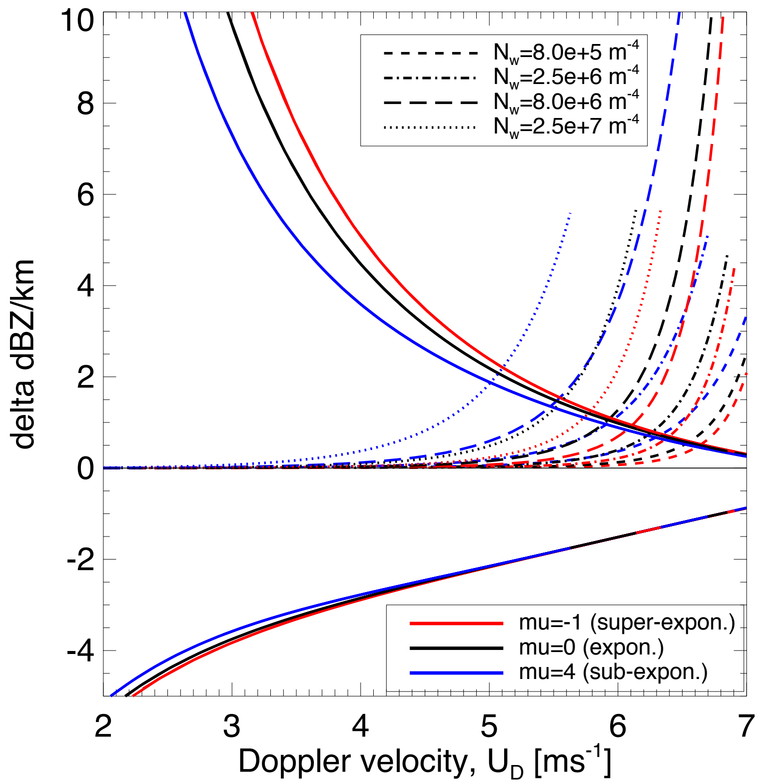

Fig. 3. Theoretical curves of the reflectivity gradient vs. the Doppler velocity at the Ka-band frequency for different rain parameters.

AMTD

7, 1807–1833, 2014

Automated rain rate estimates using the Ka-band ARM Zenith Radar (KAZR)

A. Chandra et al.

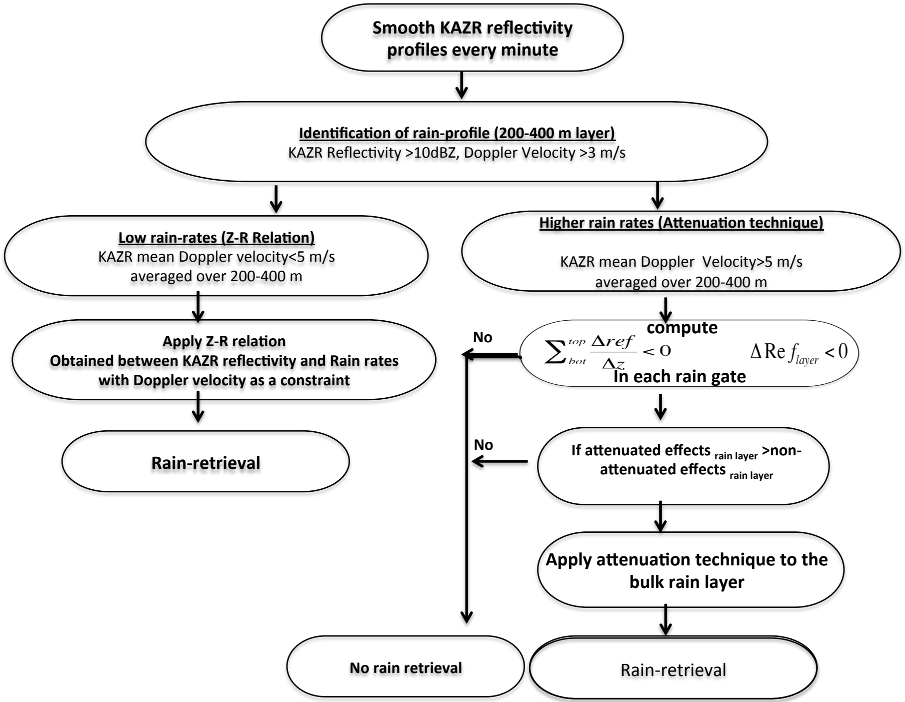

Fig. 4. Flowchart showing the sequential steps for retrieving rain rates from KAZR observations.

AMTD
7, 1807–1833, 2014

Automated rain rate estimates using the Ka-band ARM Zenith Radar (KAZR)

A. Chandra et al.

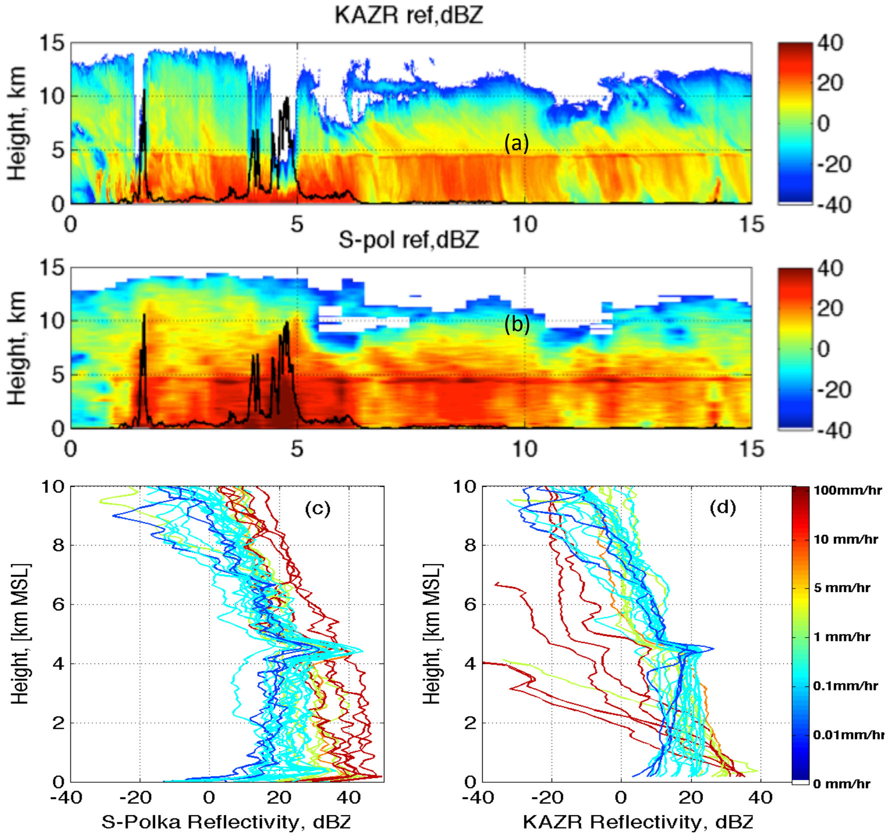

Fig. 5. Illustration of rainfall-rate retrieval under a stratiform rain condition. **(a)** Time-height plot of reflectivity values from KAZR. **(b)** Time-height plot of reflectivity values from S-Polka. **(c)** Reflectivity profiles of S-Polka for different rain rates. **(d)** Reflectivity profile of the KAZR for different rain-rates.

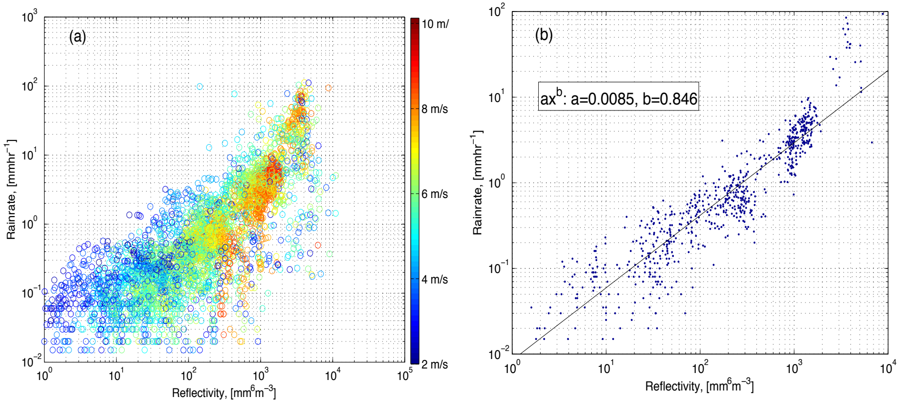

Fig. 6. Scatter plots of rain rates (R) observed from a video disdrometer vs. reflectivity values (Z_e) of the KAZR averaged between a 200–400 m layer as a function of KAZR Doppler velocities **(a)** without correction, and **(b)** with correction.

AMTD
7, 1807–1833, 2014

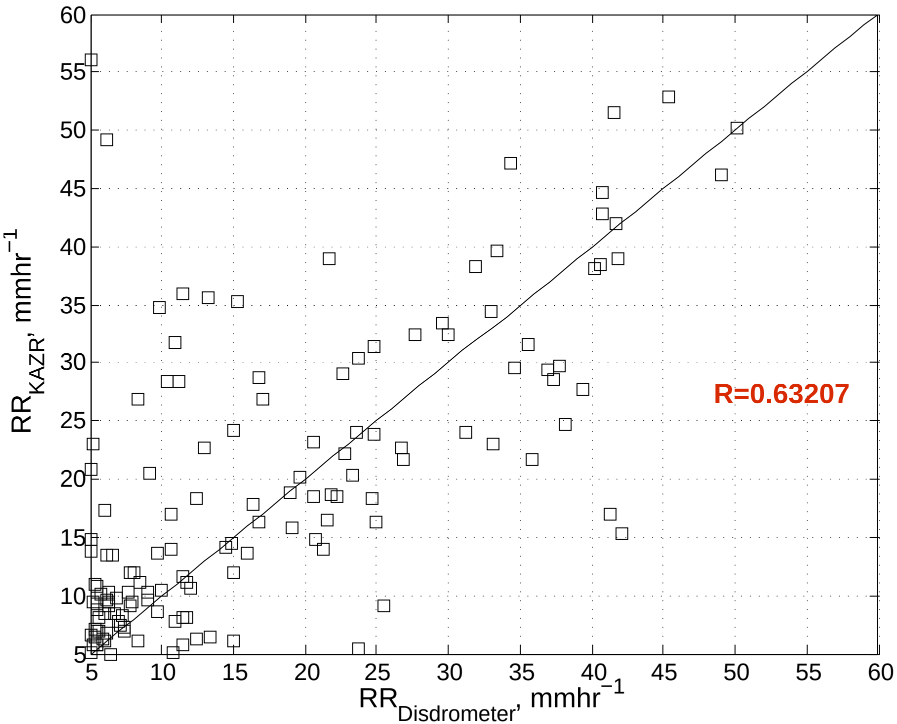

Fig. 7. Scatter plot of observed rain rates from a video disdrometer vs. rain rates retrieved from the KAZR.

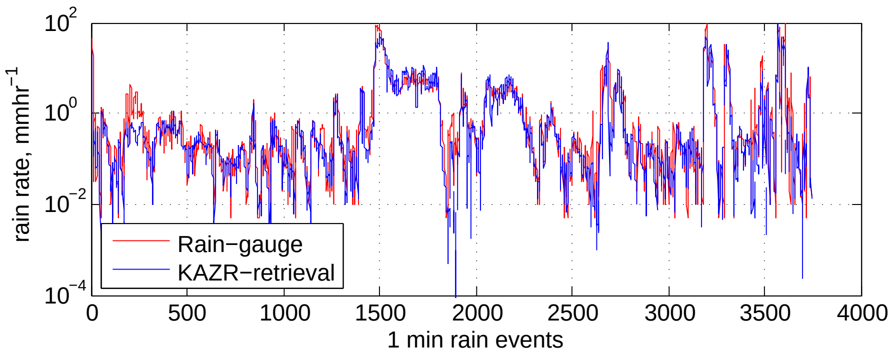

Fig. 8. Time series (8 October 2011 to 6 February 2012) of 1 min averaged rain rates from KAZR and a rain gauge.

AMTD
7, 1807–1833, 2014

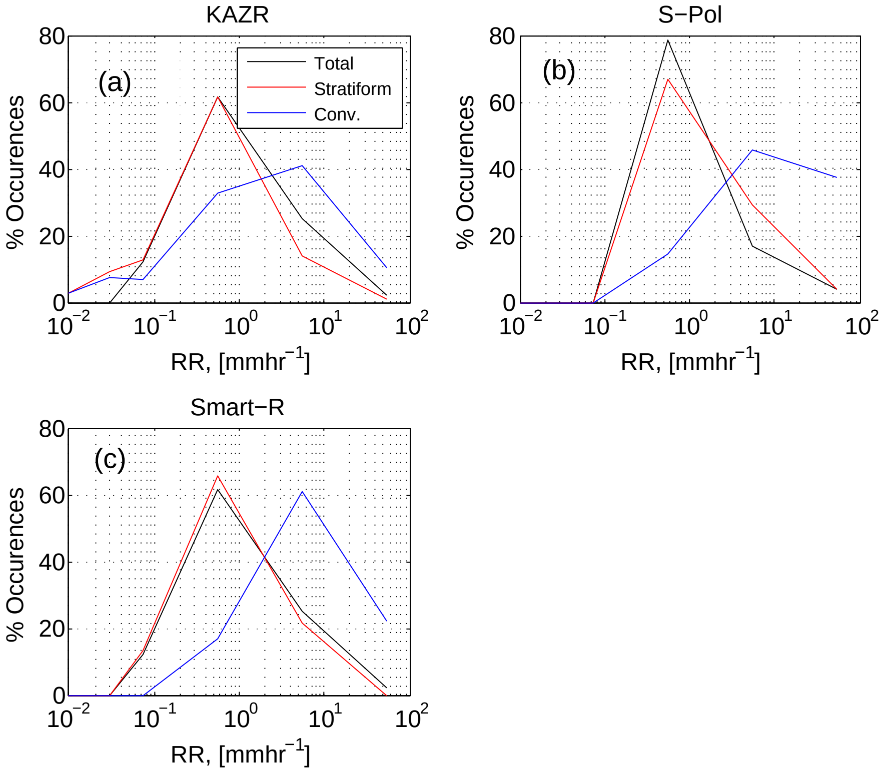

Fig. 9. Histograms of rain-rates observed under stratiform and convective conditions from **(a)** KAZR **(b)** S-polka and **(c)** SMART-R.

AMTD
7, 1807–1833, 2014